DOI: https://doi.org/10.14311/TPFM.2025.027

SIMULATION OF COMPLIANCE IN A HUMAN CAROTID ARTERY WITH RESISTANCE BOUNDARY CONDITIONS

K. Richter [1], T. Probst [1,2], A. Hundertmark [1]

[1] **Institute of Mathematics, Faculty of Natural and Enviromental Sciences, University of Kaiserslautern-Landau, Fortstraße 7, 76829 Landau, Germany**

[2] **Institute of Mathematics, Johannes Gutenberg-University Mainz, Staudingerweg 9, 55128 Mainz, Germany**

Abstract

The subject of this study is to model the physiologically realistic volumetric compliance of a human carotid artery within a fluid-structure-interaction (FSI) simulation. Computed Tomography Angiography (CTA) scans of a patient's carotid artery are used to create a virtual twin geometry of a computational domain for fluid volume and vascular tissue. In vitro silicon replicas are used to validate the stress-strain relationship of the material used and to validate the simulation with laboratory compliance tests. Subsequently, a strain-dependent Young's modulus is embedded in a high-fidelity vessel simulation to adapt the linear elasticity model to the measured vessel inflation. Resistance outlet boundary conditions are derived in the FSI context and are applied to model the physiological flow and pressure waves. As a result of this study, the natural mechanics of arteries during the cardiac cycle, the *Windkessel effect*, is observed.

Keywords: artery compliance, fluid-structure interaction, linear elasticity, resistance boundary conditions, Windkessel effect.

1 Introduction

The ability of the vessel wall to store kinetic energy and distribute fluid forces over the wall tissue, the so called *Windkessel effect*, has a serious impact on the blood dynamics response in hemodynamic modeling and therefore on the evaluation of disturbed flow patterns and shear stress predictors, linked to atherosclerotic promotion [1, 2]. The interplay between fluid and solid tissue dynamic is captured using fluid-structure interaction (FSI) models, see [3, 4, 5] to refer a few of them. Considering the significant influence of wall deformability on blood flow dynamics and surface risk indicators, incorporating realistic compliance modeling is crucial for accurate hemodynamic validation. Simulations should mimic the essential function of the arterial wall as a energy storage reservoir for converting the mechanical into elastic energy, the *Windkessel effect*.
In this study, we develop a physiological compliance model with resistance boundary conditions for the wall instead of the widely used zero stress boundary conditions [6], which do not adequately represent the physiological pressure waves, as will be shown. Our model is based on tensile tests and compliance investigations of a fabricated in vitro model of a patient-specific sealed carotid artery phantom with a stenotic occlusion region. In our approach, we **first** in-silico reproduce the experimental compliance behavior of a inflated carotid phantom with two main branches sealed off. We assess our computational model of the sealed geometry setup by evaluating the volumetric compliance as well as pressure-volume curves in respect to the in vitro model. The evaluation of diametric distensibility can be found in [7]. To enhance the conformity between our simulations and the laboratory experiments, we introduce the dependency of the elastic modulus on a strain metric, derived from the measured stress-strain relation. In a **second** step we apply our material model to a simulation of a physiological carotid artery model, which incorporates the downstream region of the cardiovascular system. A temporal and flow-dependent resistance value for the outflow boundaries and the vessel wall is implemented. This approach ensures a proper distribution of flow volume through the bifurcation and outlets while maintaining physiological pressure ranges throughout the cardiac cycle, realistically capturing the *Windkessel effect*.

2 Mathematical and numerical model

2.1 Computational geometry of the human artery

The geometry has been extracted from clinical CT scans of one individual using the open source software CarotidAnalyzer [8]. Detailed description of the geometric construction of the flow lumen and the vessel wall can be found in our previous work [7]. Two geometry domains have been derived for this study. The first is a simplified patient carotid artery with sealed outlets to validate compliance behavior. Wall thickness has been artificially increased to reduce the risks of fissure during the molding process in laboratory experiments, see Fig. 1. The second is a high-fidelity model of the patient's vessel tree structure with accurate sub-branching of the internal (ICA) and external carotid artery (ECA) leading to four outlets, cf. Fig. 2.

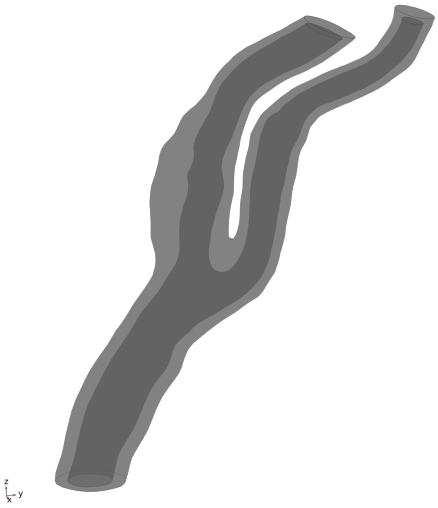

Figure 1: Simplified geometry with thick walls and sealed ICA and ECA outlets.

Figure 2: Original CA geometry with four outflows and realistic wall thickness.

2.2 Blood flow and solid deformation

In this study the blood flow is modeled based on the incompressible Navier-Stokes equations with Newtonian behavior. The Arbitrary Lagrangrian-Eulerian (ALE) formulation takes the spatial deformation of the fluid domain Ω_t^f into account. With the mesh velocity written as $\boldsymbol{w}$, we have

$$\rho_f \frac{D\boldsymbol{u}}{Dt} + \rho_f\big((\boldsymbol{u}-\boldsymbol{w})\cdot\nabla\big)\boldsymbol{u} = \nabla\cdot\boldsymbol{T}_f, \quad \nabla\cdot\boldsymbol{u} = 0 \quad \text{in} \quad \Omega_t^f, \tag{1}$$

where $\boldsymbol{u}$ is the fluid velocity, $\boldsymbol{T}_f = -p\boldsymbol{I} + 2\mu\boldsymbol{D}(\boldsymbol{u})$ the Cauchy stress tensor and $\rho_f = 1\ \mathrm{g}\cdot\mathrm{cm}^{-3}$ the constant fluid density. The mechanics of the arterial wall is modeled via the deformation of a homogeneous, isotropic and linear elastic material. With respect to the reference domain Ω_0^s the governing equations are written as

$$\rho_s \frac{\partial^2 \boldsymbol{d}}{\partial t^2} = \nabla\cdot\boldsymbol{P}^T \quad \text{in } \Omega_0^s, \text{ with} \quad \boldsymbol{P} = J\,(\boldsymbol{C}:\boldsymbol{\varepsilon})\,\boldsymbol{F}^{-T} \tag{2}$$

where $\boldsymbol{d}$ is the structural deformation and $\boldsymbol{F} = \frac{\partial x}{\partial X},\ x \in \Omega_t^s,\ X \in \Omega_0^s$ denotes the deformation gradient. $\boldsymbol{P}$ is the first Piola-Kirchhoff tensor and $J = det\boldsymbol{F}$. In this formulation, the Green-Lagrange strain is defined as $\boldsymbol{\varepsilon} = \frac{1}{2}(\boldsymbol{F}^T\boldsymbol{F} - \boldsymbol{I})$. The elasticity tensor, $\boldsymbol{C}$, is dependent on the Young's modulus E and the Poisson's ratio ν. Consequently and to incorporate the realistic stress-strain relation of the wall tissue material, we use a strain-dependent Young's modulus based on laboratory tensile tests for silicone (Dragon Skin 10 NV, Smooth-On Inc., PA, USA). Material preparation and processing as well as tensile stress-strain testing and the definition of the strain-dependent elasticity modulus E are explained in more detail in the respective sections of [7].

Fluid-structure interaction

The continuity of velocities and forces at the fluid-structure boundary is ensured by coupling conditions that enforce the balance of velocities and stresses between the fluid and the solid material:

$$\frac{\partial \boldsymbol{d}}{\partial t} = \tilde{\boldsymbol{u}} = \boldsymbol{w} \quad \text{and} \quad J\tilde{\boldsymbol{T}}_f \boldsymbol{n}_f = -\boldsymbol{P}^T \boldsymbol{n}_s \quad \text{on } \Gamma_{fsi}, \tag{3}$$

where $\tilde{\boldsymbol{u}}$, $\tilde{\boldsymbol{T}}_f$ are the fluid velocity and Cauchy-Stress tensor transformed to the fluid-solid interface in the reference frame Ω_0^f.

2.3 Resistance boundary conditions

The outflow boundary conditions of the opened artery simulation account for the resistance of the downstream arterial domain by incorporating *time-varying resistances* at the vessel outlets. This approach follows the method proposed in [9] for implementing resistance boundary conditions in a rigid wall simulation. At first, the mean volume flow Q_{mean} of one cardiac cycle and the mean pressure necessary to drive the flow is calculated, following [10]. Here, the physiological inflow function $\boldsymbol{u}_{phys}(t)$ integrated over the inlet boundary results in a cardiac output of 430 ml/min and $p_{mean} = (p_{sys} + 2 \cdot p_{dias})/3 \approx 93$ mmHg with systolic $p_{sys} = 120$ mmHg and diastolic $p_{dias} = 80$ mmHg pressure values. The total resistance, R_{tot}, of the vessel domain is directly proportional to the mean pressure, p_{mean}, is required to sustain the volume flow rate, Q_{mean}. This relationship is expressed as $p_{mean} = Q_{mean} \cdot R_{tot}$, [11]. As a novelty and in addition to the total resistance R_{out} of the internal and collective external carotid artery outlets, we attribute a time-dependent resistance $R_{wall}(t)$ to the vessel wall. Both resistances behave like resistors in parallel and contribute to the collective total resistance

$$R_{tot} := \left(\frac{1}{R_{out}} + \frac{1}{R_{wall}(t)} \right)^{-1}. \tag{4}$$

It should be noted, that in the case of rigid wall simulations the last term vanishes due to infinite wall resistance. To derive the resistance value R_{int} for the ICA outlet and R_{out} for the collective ECA outlets and account for vessel inflation we follow **3** assumptions:

1. Flow volume separation between internal and external artery is assumed in a ratio of 70:30,
$$R_{int} = \frac{1}{0.7} R_{out} \text{ and } R_{ext} = \frac{1}{0.3} R_{out},$$
2. the outflow volume through the external subbranches are proportional to their cross-sectional outlet area,
$$R_{ext_k} = \frac{\sum_{i=1}^{3} |\Gamma_{ext_i}|}{|\Gamma_{ext_k}|} R_{ext}, \text{ for } k = 1, 2, 3,$$
3. the resistance of the vessel wall is inversely proportional to the artery's capacity to store additional fluid volume when inflated or to release fluid when contracted,
$$R_{wall}(t) = \frac{\overline{p}(t)}{Q_{wall}(t)} = \frac{\frac{1}{|\Omega_f|} \int_{\Omega^f} p(t)\, dV}{\int_{\Gamma_{fsi}} \dot{\boldsymbol{d}}(t) \cdot \boldsymbol{n}_f \, dS}.$$

Here, $\overline{p}(t)$ is the current, averaged pressure in the fluid domain $\Omega^f(t)$ and $Q_{wall}(t)$ is the volume flow rate arising from wall deformation, i.e. the vascular capacity of the computational arterial domain. Finally, the outlet resistance boundary conditions replace the outlet pressures by

$$p_{ext_k} = -R_{ext_k} \int_{\Gamma_{ext_k}} \boldsymbol{u}(t) \cdot \boldsymbol{n}_f \, \mathrm{dS} \quad \text{on } \Gamma^f_{ext_k}, \text{ for } k = 1, 2, 3, \tag{5}$$

where $\boldsymbol{n}_f$ is the fluid outer normal. For the remaining boundary conditions, we impose zero displacement on the inlet and outlet surfaces of the artery. The exterior vessel wall is allowed to move freely under zero-stress conditions. The time-dependent flow velocity, $\boldsymbol{u}_{phys}(t)$, corresponding to a typical volumetric flow rate pulse wave, is prescribed at the inlet of the carotid artery, as described in [12].

2.4 Numerical solver

The coupled FSI problem (1) – (3) is numerically solved using the finite-element-based software COMSOL Multiphysics 6.1, employing the Structural Mechanics Module with a monolithic, fully coupled FSI approach. Linear P1-P1 elements are utilized for fluid discretization, while quadratic serendipity elements are used for modeling solid deformation. The computational mesh, including two boundary layers, comprises approximately $1.34 \cdot 10^5$ tetrahedral elements for the fluid domain and $4.1 \cdot 10^4$ prism elements for boundary layers. Additionally, a mesh increasing factor of 1.2 for gradual enlargement of the neighboring inward mesh elements is applied resulting in a local refinement of the boundary layer region. The solid domain is discretized into approximately $1.06 \cdot 10^5$ tetrahedral elements. The numerical convergence of the solution is validated in a mesh refinement study of the sealed artery by comparing solutions for a sequence of five non-uniform meshes from $2.7 \cdot 10^4$ to $4.4 \cdot 10^5$ total elements to a reference solution on a mesh containing $1.7 \cdot 10^6$ elements. For computational cost reasons, the consecutive grids are not generated by refining the previous mesh elements. Instead, they are newly constructed by defining the next smallest and largest mesh element size, resulting in non-coinciding nodes between different grids; to evaluate the error, the solutions have been interpolated between the grids. The experimental order of convergence, defined as the slope of error decrease curves with respect to the mean mesh size, presented in Fig. 3, confirms the almost linear convergence for the flow velocities, quadratic convergence for the wall deformation and third-order convergence for the pressure field towards the reference solution.

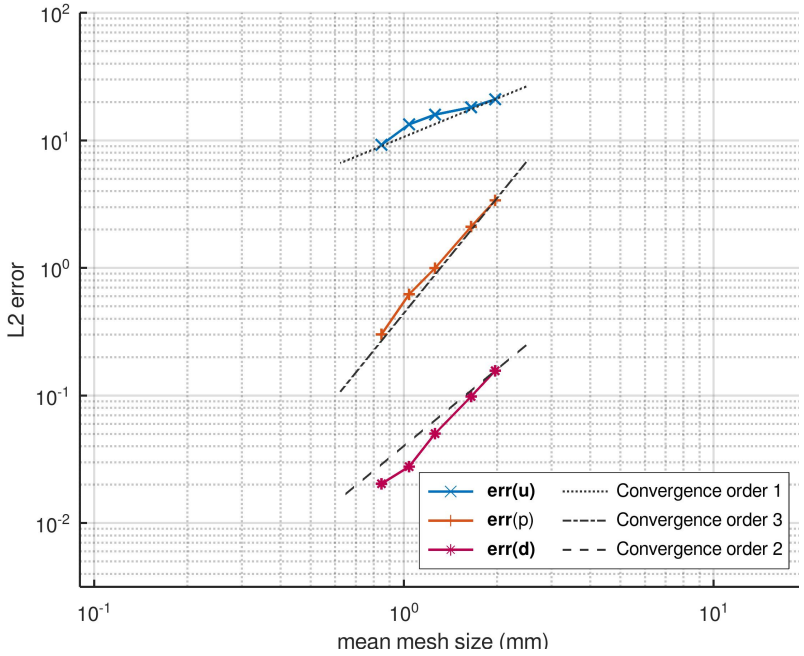

Figure 3: Decrease of L_2 errors w.r. to mean mesh size for velocity, pressure and wall deformation at time $t = 0.11s$ and approximately 140 mmHg.

3 Compliance of sealed carotid bifurcation

Data from laboratory experiments with sealed carotid bifurcation phantoms are utilized to develop a physiological in silico compliance model. These results reveal a highly non-linear behavior between induced stress through uniaxial strain in the material, Fig. 4. The non-linear, strain-dependent Young's modulus function $E(\varepsilon)$, shown in Fig. 5, is derived from uniaxial tension tests by calculating the slope of the experimental stress-strain curves presented in Fig. 4. This function is then incorporated into our 3D simulation model with a sealed geometry. Hereby, the Cauchy stress tensor $\boldsymbol{\sigma} = \boldsymbol{C}(E, \nu) : \boldsymbol{\varepsilon}$ in the elasticity model (2) is dependent on the same strain metric as $E(|\boldsymbol{\varepsilon}|)$. Here $|\boldsymbol{\varepsilon}| := \frac{\gamma}{\sqrt{2}(1+\nu)} + \frac{\boldsymbol{\varepsilon}_{vol}}{3} \frac{1}{1-2\nu}$ is chosen to account for both volumetric strain

$\boldsymbol{\varepsilon}_{vol} = trace(\boldsymbol{\varepsilon})$, as well as the shear (deviatoric) strain $\gamma = \sqrt{2\ dev(\boldsymbol{\varepsilon}) : dev(\boldsymbol{\varepsilon})}$, $dev(\boldsymbol{\varepsilon}) := \boldsymbol{\varepsilon} - \frac{\boldsymbol{\varepsilon}_{vol}}{3}$, see [7]. In the numerical simulation of the sealed artery inflation we observe an exponential relationship between fluid pressure and inflated artery volume for the generalized elasticity model with adapted strain-dependent Young's modulus (red dashed curve), see Fig. 6. This behavior is also reflected in the experimental curves (dotted curves), particularly in the investigated pressure range including the systolic and diastolic phases, whereas the almost linear pressure-volume curve of the pure linear elasticity model (blue curve) does not sufficiently reflect the experiments in this pressure range. This confirms the improvement of our generalized elasticity approach. Moreover, comparing the clinically relevant volumetric compliance parameter $C_{p_1-p_2}$, defined as the relative slope of the pressure-volume curves, see [7], at diastolic/systolic pressures $p_1 = 80$ mmHg, $p_2 = 120$ mmHg, shows a clear trend of our generalized approach towards the experimental measurements with compliance values $C_{80-120} = 0.247, 0.275, 0.330$ for linear elasticity, generalized elasticity with $E(|\boldsymbol{\varepsilon}|)$ and experimental compliance, respectively. The spatial distribution of the strain, depicted in Fig. 7 explains an elevated volume increase of our generalized model. Indeed, due to the strain dependency of the elasticity modulus E, regions of higher strains are more deformable resulting in a higher volume increase.

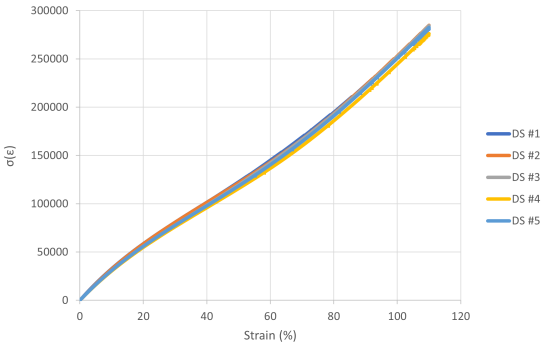

Figure 4: Experimental stress-strain curves for uniaxial strain $\sigma(\varepsilon)$ with five phantoms.

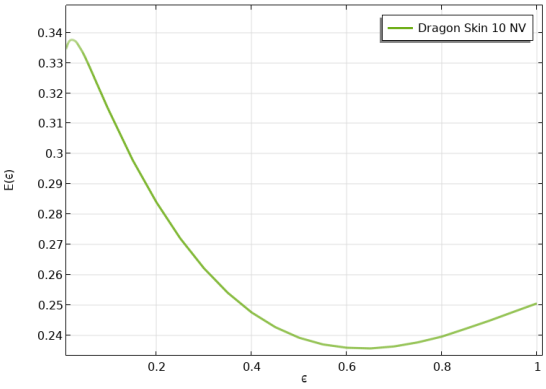

Figure 5: Young's modulus $E(\varepsilon)$ extracted as a local tangential slope of the measured uniaxial stress-strain curve (in MPa).

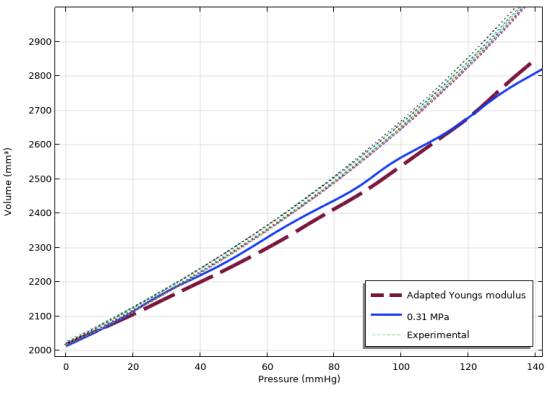

Figure 6: Experimental and simulated pressure-volume curves for linear and adapted elasticity model with variable Young's modulus.

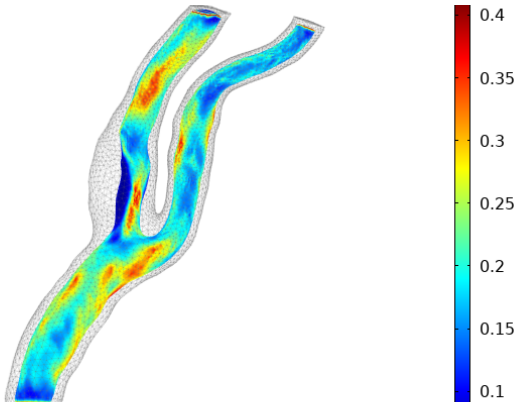

Figure 7: Surface distribution of the strain quantity $|\boldsymbol{\varepsilon}|$ at 140 mmHg.

To supplement the mesh convergence study mentioned in section 2.4, the numerical convergence of the artery volume is also evaluated in the context of volumetric compliance. By studying the relative differences of the artery volume for two subsequent meshes, reached at systolic pressure of 120 mmHg, $\frac{V^{(i)} - V^{(i-1)}}{V^{(i)}}$, $i = 1, \ldots, 7.$, we calculated an error decrease from 1.22% for mesh

no. 1 and 2 to 0.125% for mesh no. 6 and 7. Based on the presented experimental validation of the numerical model in sealed artery inflation, the generalized elasticity material approach is transferred to our further investigations of the opened carotid artery.

4 Results on the compliance in open carotid artery

In this section, the numerical results of the compliant artery model with resistance boundary conditions (4)-(5) at the outlets of the original carotid geometry, see Figure 2, is presented. The effects of this approach are compared to the widely used zero stress outflow boundary condition $\boldsymbol{T}_f \boldsymbol{n}_f = 0$. This comparison aims to assess the physiological accuracy of our model in regard to volumetric compliance and pressure waves.

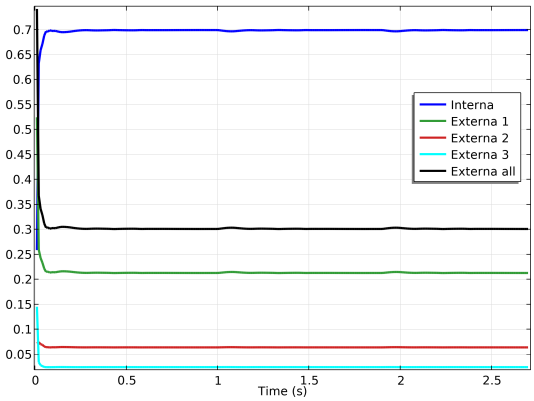

Figure 8: Proportion of the total flow volume that exits through ICA/ECA outlets in the simulation of three cardiac cycles with resistance boundary condition is in conformity with prescribed blood flow distribution.

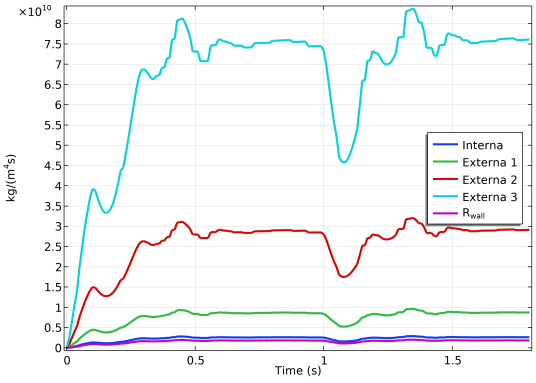

Figure 9: Time-dependent resistance values for the ICA and ECA outlets R_{int}, R_{ext} and the resistance of the vessel wall R_{wall} during the first two cardiac cycles.

Firstly, we present the time-dependent resistance values imposed on the four outlets of the original CA geometry and the vessel wall in Fig. 9. Here, we can observe the resistance dynamics driven by the pulsating inlet velocity and the flow splitting in daughter branches, see, Fig. 8, following the principles described in section 2.3. Smaller outflow surfaces are attributed a lower outflow volume and therefore yield a higher resistance to the flow dynamics. During systole (at time 1.1s) the flow volume increases and we observe a decrease in all outlet resistances. This phenomenon is reversed during diastole.

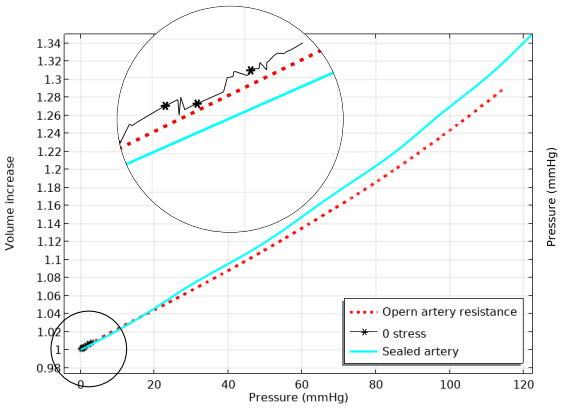

Figure 10: Relative pressure-volume curves compared for a sealed artery and for opened artery applying resistance and zero stress outlet boundary conditions.

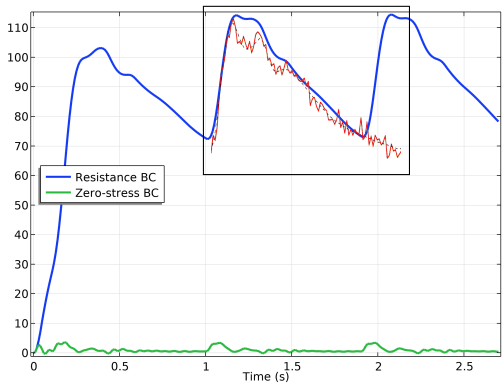

Figure 11: Mean pressure obtained with resistance and zero stress boundary conditions compared to in vivo measurements (red and denoised in black dotted) from [13] to confirm suitability of the resistance BC approach.

The pressure-volume curves for the open artery simulation using our approach exhibit compliance behavior that closely mirrors that of the sealed artery compliance, see Fig. 10. Both simulations reach physiologically expected pressure values, with a similar increase in artery volume. The open artery model with zero stress boundary conditions, on the other hand, does not remotely reach physiological pressure levels. Starting from zero initial conditions and over the time of 2 cardiac cycles, the pressure in the resistance BC simulation adjusts to a physiological pressure wave, whereas the zero stress BC simulation fails to exhibit this behavior, see Fig. 11. Values below 5 mmHg and the lack of volume increase show the inability of the zero stress boundary conditions to incorporate the crucial capacity behavior of the cardiovascular system. The use of resistance boundary conditions lead to physiological pressure waves, matching with pressure waves observed in the carotid bifurcation obtained in vivo by Bikia et al. [13].

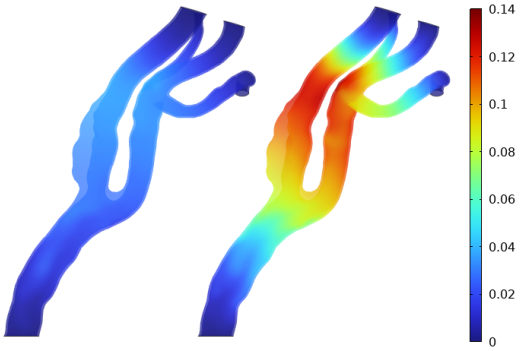

Figure 12: Surface displacement (in mm) for zero stress boundary conditions for diastolic (left) and systolic (right) pressure.

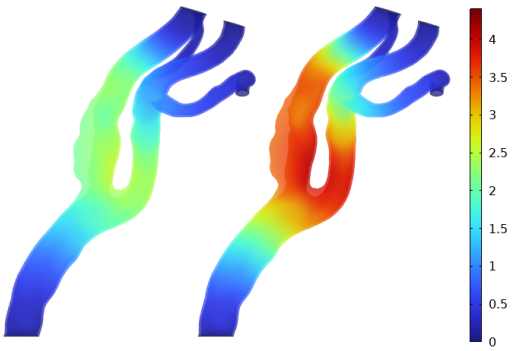

Figure 13: Surface displacement (in mm) for resistance boundary conditions for diastolic (left) and systolic (right) pressure, showing significantly higher deformations and stronger inflation effect.

Corresponding to those physiological pressure waves, the resistance model inflates in systole and deflates in diastole, with displacement values of around 2 mm for diastolic and over 4 mm for systolic pressure, where the zero stress model only reaches displacement values of 0.04 mm to 0.14 mm, see Figs. 12, 13.

5 Conclusion

In this study, the compliance behavior of a patient-specific carotid bifurcation with stenotic occlusion was numerically modeled. An adapted elasticity model for the vascular tissue was derived from in vitro experiments with a sealed carotid artery phantom. The observed non-linear stress-strain relationship was implemented using a strain-dependent elastic modulus. In doing so, we obtained the desired exponential behavior in volume increase with respect to pressure, i.e. the volumetric compliance of the material. Other materials and laboratory tensile tests therefore, can be easily implemented in future research and simulations, where exact compliant behavior over a large pressure scale is required. The proposed time-dependent resistance outlet boundary conditions for an open compliant patient carotid artery with multiple outflows effectively regulate the flow splitting. Our approach accounts for the physiologically observed ECA-ICA flow splitting at the bifurcation and incorporates the additional resistance from vessel wall deformation within the context of FSI. We showed, that this flow distribution is enforced in every time step of our transient study, whereby a looser restriction could be favorable in physiological simulations. The compliance results demonstrate the effectiveness of our approach, showing strong agreement of the compliance behavior with in vitro data on sealed artery compliance. Additionally, there is a good correlation between our numerically reconstructed pressure ranges and pulse waves, which closely align with physiological pressure waves, effectively representing the *Windkessel effect*.

Acknowledgement

This work was funded by the BMBF joint Project 05M20UNA-MLgSA.

References

[1] Xiang, J., Sabareesh, K., Natarajan, S.K., Tremmel, M., Ma, D., Mocco, J., Hopkins, L.N., Siddiqui, A.H., Levy, E.I., & Meng, H.: Hemodynamic-morphologic discriminants for intracranial aneurysm rupture. *Stroke*, vol. 42, no. 1: (2011) pp. 144–152.

[2] Hoogendoorn, A., Kok, A.M., Hartman, E.M.J., de Nisco, G., Casadonte, L., Chiastra, C., Coenen, A., Korteland, S.-A., Van der Heiden, K., & Gijsen, F.J.H.: Multidirectional wall shear stress promotes advanced coronary plaque development: comparing five shear stress metrics. *Cardiovascular Research*, vol. 116, no. 6: (2020) pp. 1136–1146.

[3] Colciago, C.M., Deparis, S., & Quarteroni, A.: Comparisons between reduced order models and full 3D models for fluid–structure interaction problems in haemodynamics. *Journal of Computational and Applied Mathematics*, vol. 265: (2014) pp. 120–138.

[4] Holzapfel, G.A., Gasser, T.C., & Ogden, R.W.: A New Constitutive Framework for Arterial Wall Mechanics and a Comparative Study of Material Models. *Journal of Elasticity*, vol. 61: (2000) pp. 1–48.

[5] Torii, R., Oshima, M., & Kobayashi, T.: Fluid–structure interaction modeling of a patient-specific cerebral aneurysm: influence of structural modeling. *Computational Mechanics*, vol. 43: (2008) pp. 151–159.

[6] Ayodele, J.O., Awonusi, A.A., & Ige, E.O.: Fluid-structure interaction study of hemodynamics and its biomechanical influence on carotid artery atherosclerotic plaque deposits. *Medical Engineering and Physics*, vol. 117: (2023) pp. 103998.

[7] Shiravand, A., Richter, K., Willmann, P., Eulzer, P., Lawonn, K., Hundertmark, A., & Cattaneo, G.: Fabrication, characterization and numerical validation of a novel thin-wall hydrogel vessel model for cardiovascular research based on a patient-specific stenotic carotid artery bifurcation. *Scientific Reports*, vol. 14, no. 1: (2024) pp. 16301.

[8] Pepe, E.: Carotid Analyzer Pipeline. *Available online:* https://github.com/PepeEulzer/CarotidAnalyzer/, [Accessed: 19-December-2024].

[9] Vignon-Clementel, I.E., Figueara, A.C., Jansen, K.E., & Taylor, C.A.: Outflow boundary conditions for three-dimensional finite element modeling of blood flow and pressure in arteries. *Computer Methods in Applied Mechanics and Engineering*, vol. 195, no. 29: (2006) pp. 3776–3796.

[10] Levick, J. Rodney: An introduction to cardiovascular physiology. *Butterworth-Heinemann*, (2013).

[11] Pape, H.-C. & Kurtz, A.: Physiologie (Silbernagl), 9. Auflage. *Thieme*, (2014).

[12] Richter, K., Hundertmark, A., Probst, T., Eulzer, P., & Lawonn, K.: Longitudinal wall shear stress evaluation using centerline projection approach in the numerical simulations of the patient-based carotid artery. *Computer Methods in Biomechanics and Biomedical Engineering*, vol. 27, no. 3: (2023) pp. 1–18.

[13] Bikia, V., Segers, P., Rovas, G., Pagoulatou, S., & Stergiopulos, N.: On the assessment of arterial compliance from carotid pressure waveform. *American Journal of Physiology-Heart and Circulatory Physiology*, vol. 321, no. 2: (2021) pp. H424–H434.